JCTC Journal of Chemical Theory and Computation

pubs.acs.org/JCTC Article

Computational Design Strategy for Aggregation-Induced Emission Luminogens: Modulating the S_1/S_0 Minimum Energy Conical Intersection of Anthracene Derivatives through Substituent Effects

Published as part of Journal of Chemical Theory and Computation special issue "Developments of Theoretical and Computational Chemistry Methods in Asia".

Ping-An Yin, Qi Ou,* and Zhigang Shuai*

Cite This: J. Chem. Theory Comput. 2025, 21, 4992−5002 Read Online

ACCESS | Metrics & More | Article Recommendations | Supporting Information

ABSTRACT: Aggregation-induced emission (AIE) has become a key focus in luminescent material development, with substituent modulation being a critical strategy for expanding AIE systems. The S_1/S_0 minimum energy conical intersection (MECI) significantly influences molecular photophysical properties, making it essential for understanding the AIE phenomenon. Here, we employ anthracene derivatives, known for their chemical versatility and applications in organic light-emitting diodes (OLEDs), to systematically investigate the effects of substituents on the S_1/S_0-MECI. We select 22 anthracene derivatives with varied electron-donating and electron-withdrawing substituents and explore their impacts on the S_1/S_0-MECI relative energy and molecular structure. Our findings reveal that strong electron-donating or electron-withdrawing groups at the C9-position effectively lower the S_1/S_0-MECI relative energy of the gaseous phase singly substituted anthracene derivatives, thus enhancing the AIE phenomenon of such molecules. Additionally, doubly substituted derivatives on the same ring also slightly reduce the S_1/S_0-MECI relative energy of the isolated molecule. Based on these insights, we propose a novel AIE molecular design strategy focusing on modulating S_1/S_0-MECI through strategic substituent selection, leading to the identification of 24 AIEgens candidates among 81 anthracene derivatives. In summary, our study provides a systematic approach to designing AIE molecules by modulating the S_1/S_0-MECI through a substituent effect. The validity of this strategy is confirmed using the 9-tBu-Ant molecule with quantitative calculations.

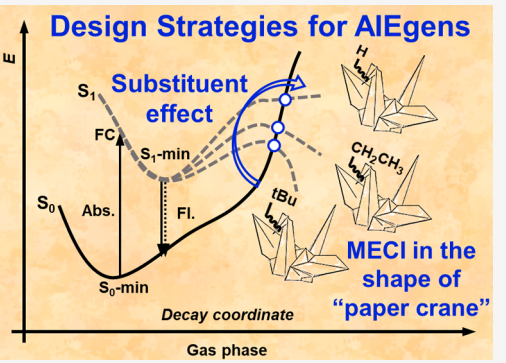

1. INTRODUCTION

In 2001, Tang's group discovered that polyphenyl-substituted silole derivatives exhibit significantly enhanced emission in the aggregated state, leading to the introduction of the aggregation-induced emission (AIE) concept.[1] The development and application of AIE luminogens (AIEgens) with excellent solid-phase luminescence performance have become a research focus in chemistry and materials science.[2−7] Over 24 years, AIEgens have found applications in various cutting-edge technological fields, including solid-state organic light-emitting devices (OLEDs),[8−11] bioimaging,[12−15] photodynamic therapy,[16−18] metal ion detection,[19−21] and super-resolution imaging.[22] These applications are typically problem-focused, involving the straightforward extension of classical AIEgens at the molecular level to develop materials with specific properties. Typically, the design of AIE materials is achieved through the substitution of AIE core molecules with functional groups, thereby yielding novel derivatives that exhibit AIE properties.[23−26] Taking the modification of tetraphenylethylene (TPE) as an example, a typical strategy of developing AIE materials involves substituting specific groups to introduce electron-donating or electron-withdrawing moieties at the substituent sites of the TPE phenyl ring. This approach effectively modulates the absorption and emission energies of the system while preserving the AIE characteristic, enabling the tuning of the emission peak over the entire visible and near-infrared regions.[27] In 2014, Sun et al. reported that bridging TPE with pyrrole via a phenyl ring yielded novel AIE molecules with enhanced solid-phase luminescence and red-shifted emission.[28] The simple functional groups such as aldehydes can be introduced at various sites (meta or para) on the TPE phenyl rings to synthesize mechanochromic materials

Received: February 10, 2025
Revised: April 6, 2025
Accepted: April 15, 2025
Published: April 25, 2025

https://doi.org/10.1021/acs.jctc.5c00231
J. Chem. Theory Comput. 2025, 21, 4992−5002

Scheme 1. Chemical Structures of Target Molecules

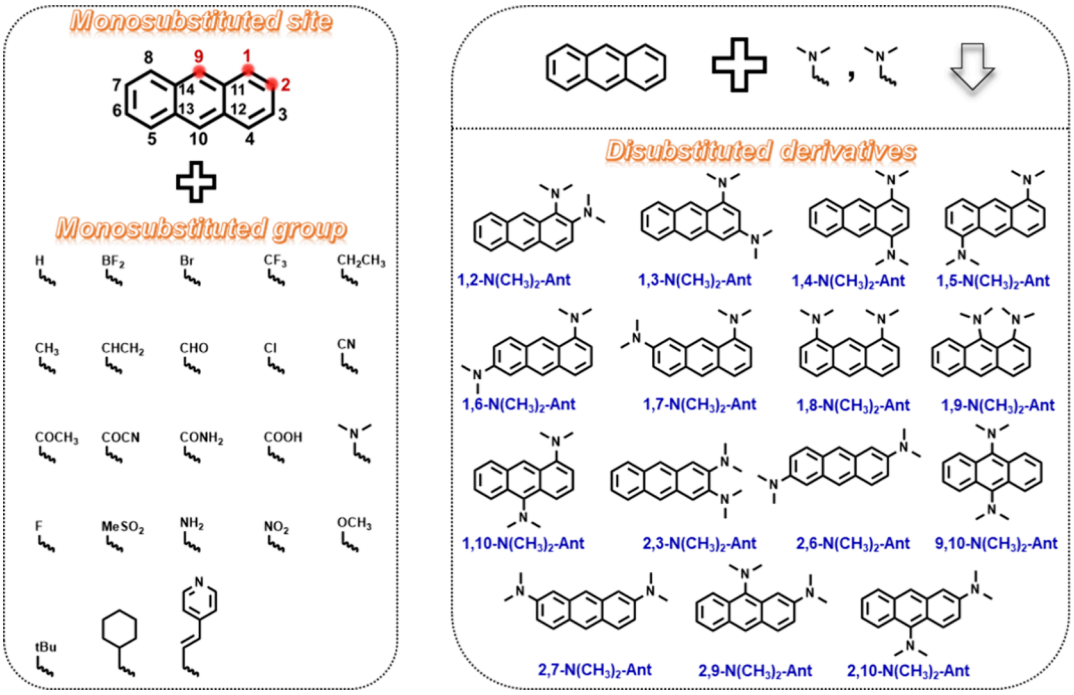

with diverse properties.[28] Similarly, nitro groups introduced for mono-, di-, tri-, and tetra-substitution on the TPE phenyl rings result in mechanochromic materials with distinct properties.[29] Furthermore, introducing methyl or methoxy groups at two substitution sites on TPE results in the formation of E/Z isomers, which are valuable for investigating the mechanisms of AIE.[30] The aforementioned TPE derivatives, similar to TPE itself, predominantly exhibit AIE phenomena that adhere to the restriction of intramolecular rotation (RIR) mechanism.[31] These examples highlight the significance of both core AIE molecules and substituent modifications in the design and development of the AIE-active compounds. However, the number of experimentally reported AIEgens that can serve as core scaffolds, such as TPE, remains limited.[32−37] Satisfying both strong chemical modifiability and a well-defined luminescence mechanism simultaneously is highly challenging and becomes a bottleneck in the expansion of AIEgens.

Quantitatively predicting the photophysical properties in both the gas and solid phases is a necessity in the design of novel AIE molecules. In our previous research, we proposed a two-channel picture[38] to quantitatively describe the nonradiative decay process of the S_1 state, with channel I the vibrational relaxation-induced nonradiative transition and channel II the nonradiative decay through an S_1/S_0 minimum energy conical intersection (MECI). Our findings indicate that the AIE phenomenon in these systems is primarily attributed to the restriction of channel II. In fact, restricting access to MECI is a classic mechanism for the explanation of the AIE phenomenon.[39] Our previous study also reveals that varying substitution sites in anthracene derivatives could modulate the relative energy of S_1/S_0-MECI, thereby affecting the photophysical properties of the system.[40]

In this work, we aim to explore novel strategies for the design of AIE core molecules by elucidating the relationship between substituents and S_1/S_0-MECI. We select anthracene as the research carrier. As one of the earliest studied blue fluorescent dyes, anthracene possesses multiple substitutable sites, similar to TPE, and exhibits strong chemical modifiability. Herein, anthracene serves as the core scaffold, and 22 substituents with diverse electron donor−acceptor (EDA) properties are selected for investigation. Our findings reveal that strong electron-donating or electron-withdrawing groups at the C9-position effectively lower the S_1/S_0-MECI relative energy of the gaseous phase singly substituted anthracene derivatives, thus enhancing the AIE phenomenon of such molecules. Additionally, doubly substituted derivatives on the same ring also slightly reduced the S_1/S_0-MECI relative energy of the isolated molecule. Based on these insights, we propose a novel AIE molecular design strategy focusing on modulating S_1/S_0-MECI through strategic substituent selection, leading to the identification of 24 AIEgens candidates from 81 anthracene derivatives. The validity of this strategy is confirmed using the 9-tBu-Ant molecule for quantitative calculations.

2. COMPUTATIONAL METHODOLOGY

Single substitutions are performed at three distinct substitutable positions on the anthracene ring (C9-, C1-, and C2-), resulting in 66 unique single-substituted anthracene derivatives. For clarity, we label the monosubstituted anthracene derivatives at the C9-, C1-, and C2-positions as 9-Sub-Ant, 1-Sub-Ant, and 2-Sub-Ant, respectively. Similarly, disubstituted anthracene derivatives are denoted as Di-Sub-Ant. The chemical structures of the anthracene derivatives are depicted in Scheme 1. Geometries for both the S_0 and S_1 states, along with the S_1/S_0-MECI, were optimized using the spin-flip time-dependent density functional theory (SF-TDDFT)[41] with the def2-SVP basis set. The SF-TDDFT approach has become the technique of choice for accurately identifying the S_1/S_0-MECI in medium to large-sized molecules, attributed to its efficient computational demands and its capability to provide a balanced and precise description of both the ground and excited states.[42] The ωB97X-D functional[43] was employed for all target molecules, with the ω parameter finely tuned for each

https://doi.org/10.1021/acs.jctc.5c00231
J. Chem. Theory Comput. 2025, 21, 4992−5002

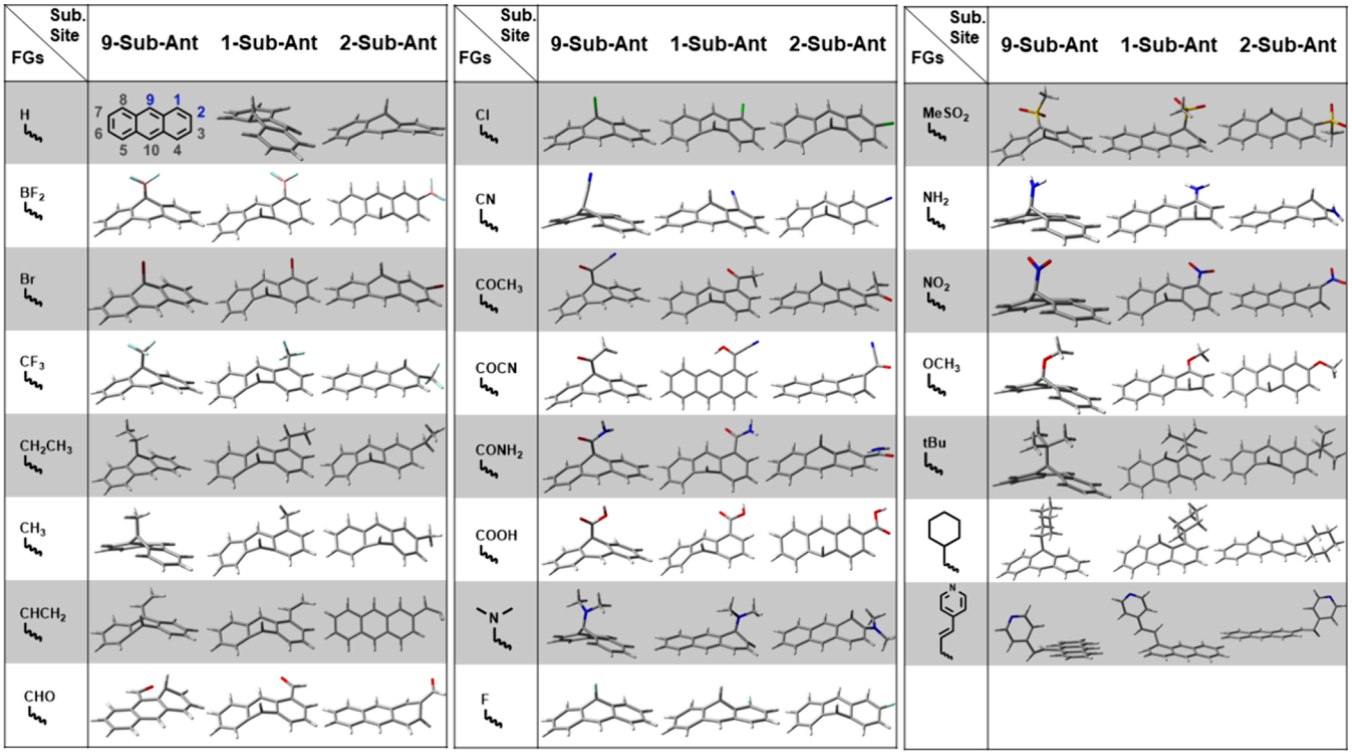

Figure 1. S_1/S_0-MECI structures of monosubstituted anthracene derivatives.

molecular system, as specified in Table S1. All electronic structure properties discussed herein were computed utilizing the quantum chemistry package Q-chem version 5.3.[44] Fluorescence spectra were simulated using the thermal vibration correlation function (TVCF) method, as implemented in the MOMAP program.[45,46] Two independent descriptors for σ- and π-substituent effects, sEDA and pEDA, were formulated employing the Natural Population Analysis (NPA) methodology.[47,48] For anthracene derivatives, sEDA and pEDA are defined as follows

$$\text{sEDA} = \sum_{j=1}^{14} \sigma^{j}_{\text{R}-\text{C}_{14}\text{H}_9} - \sum_{j=1}^{14} \sigma^{j}_{\text{C}_{14}\text{H}_{10}} \tag{1}$$

$$\text{pEDA} = \sum_{j=1}^{14} \pi^{j}_{\text{R}-\text{C}_{14}\text{H}_9} - \sum_{j=1}^{14} \pi^{j}_{\text{C}_{14}\text{H}_{10}} \tag{2}$$

where σ_i^j and π_i^j denote sums of occupancies of all atomic orbitals of the jth anthracene ring C atom contributing to the valence s- and p-molecular orbitals (respectively) in the molecule indexed by i. The NPA and vibrational frequency analysis on the optimized geometries of anthracene derivatives were performed using Gaussian 16 software, revision A.03.[49] Notably, all of the photophysical properties of anthracene derivatives in this study were calculated under vacuum conditions, with environmental effects excluded from the analysis. It is worth noting that the solid phase calculations of 9-tBu-Ant are modeled by a combined quantum mechanical and molecular mechanical (QM/MM)[50] method via the Q-Chem package, version 5.3, and the electrostatic embedding scheme is applied in the QM/MM calculations.

In our previously proposed two-channel scheme, as shown in Figure 7b, the total nonradiative decay rate k_{nr} is calculated as $k_{\text{nr}} = k_{\text{nr}}^{\text{TVCF}} + k_{\text{nr}}^{\text{MECI}}$, where $k_{\text{nr}}^{\text{TVCF}}$ and $k_{\text{nr}}^{\text{MECI}}$ represent the two nonradiative decay rates from different channels (channel I via the vibrational relaxation pathway and channel II through a S_1/S_0-MECI).[38] The transition state theory (TST)[51,52] has been introduced to quantitatively describe the influence of channel II as

$$k_{\text{nr}}^{\text{MECI}} = \frac{k_{\text{B}}T}{h}\exp\left(-\frac{\Delta G^{\neq}}{RT}\right) \tag{3}$$

where $\Delta G^{\ddagger}$ is the Gibbs free energy of activation between the S_1-min structure and S_1/S_0-MECI along the reaction path. To compute $\Delta G^{\ddagger}$, we choose the thermodynamic data at the stationary structure (S_1-min) and that at S_1/S_0-MECI. To quantitatively explore the excited state deactivation process in the AIE candidates, we calculate the radiative rates k_{r} and nonradiative rates k_{nr} of the S_1 state. The radiative rate of the S_1 state can be calculated as the integration of the light emission spectrum via the TVCF method

$$k_{\text{r}}^{\text{TVCF}} = \int_0^{\infty} \sigma_{\text{em}}(\omega)\text{d}\omega \tag{4}$$

where the emission spectrum function

$$\sigma_{\text{em}}(\omega) = \frac{4\omega^3}{3c^3}\sum_{\nu_i,\nu_f} P_{i\nu_i}(T)|\langle\Theta_{f\nu_f}|\overrightarrow{\mu_{\text{fi}}}|\Theta_{i\nu_i}\rangle|^2 \delta(E_{\text{if}} + E_{i\nu_i} - E_{f\nu_f} - \hbar\omega) \tag{5}$$

where c is the velocity of light, $P_{i\nu_i}(T)$ is the Boltzmann distribution function for the initial vibronic manifold, $\mu_{\text{fi}}\rightarrow$ is the electric transition dipole moment, E_{if} represents the adiabatic excitation energy, and $E_{i\nu_i}$ ($E_{f\nu_f}$) is the vibrational energy in the initial (final) electronic state. The nonradiative decay process in the harmonic region of the S_1 state contains two paths, i.e., internal conversion (IC) via vibrational

https://doi.org/10.1021/acs.jctc.5c00231
J. Chem. Theory Comput. 2025, 21, 4992−5002

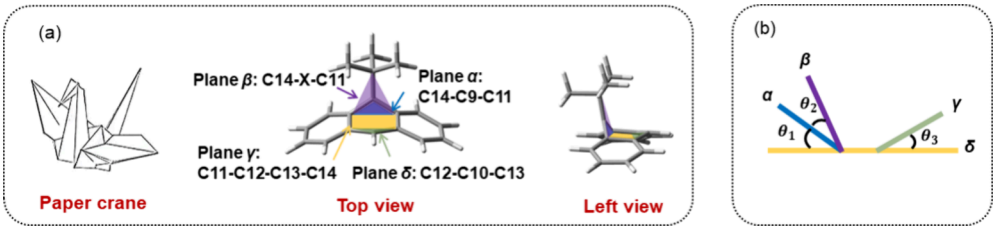

Figure 2. (a) Definitions of the plane in 9-tBu-Ant molecule; (b) schematic diagram of the dihedral angles.

relaxation (channel I) to S_0 and intersystem crossing (ISC) to T_n. Here, we neglect the influence of ISC for all investigated molecules due to the fact that no phosphorescence was experimentally observed in the reported molecules. The rate constant of the nonradiative decay process k_{nr}^{TVCF} can therefore be approximately considered as the IC rate constant as

$$k_{nr}^{TVCF} = k_{ic} = \frac{1}{\hbar^2} R_{kl} \int_{-\infty}^{\infty} dt[e^{i\omega_{if}t} Z_i^{-1}(t, T)\rho_{ic,kl}(t, T)] \quad (6)$$

where $\rho_{ic,kl}(t, T)$ is the IC thermal vibration correlation function.

The fluorescence efficiency can be easily evaluated as

$$\Phi_{fl} = \frac{k_r}{k_r + k_{nr}} \quad (7)$$

3. RESULTS AND DISCUSSION

3.1. Substituent Site and S_1/S_0-MECI. In this work, we optimize the S_1/S_0-MECI structure to investigate its geometric characteristics. The resulting S_1/S_0-MECI structures of 67 monosubstituted anthracenes, including the unsubstituted anthracene (-H), were calculated using the SF-TDDFT method, are illustrated in 1. The most pronounced S_1/S_0-MECI structural deformation observed in the majority of anthracene derivatives occurs at the C9-X position (where X represents the substituent or hydrogen). This deformation is characterized by significant out-of-plane distortion along the C9-X single bond, deviating from the plane of the anthracene ring. This unique conformational feature is reminiscent of the shape of a paper crane. In addition, some unique S_1/S_0-MECI structures of monosubstituted anthracene derivatives are discussed in Section 1 of the Supporting Information. In the 1-Sub-Ant systems, the S_1/S_0-MECI structures of 1-$N(CH_3)_2$-Ant and 1-$MeSO_2$-Ant exhibit deformation at the C1-position (substitution site), while 1-NH_2-Ant and 1-OCH_3-Ant show deformation at the C4-position (opposite the substitution site). In the 2-Sub-Ant systems, S_1/S_0-MECI structures of 2-CHO-Ant, 2-COCN-Ant and 2-NO_2-Ant display deformation at the C2-position (substitution site), whereas 2-CF3-Ant, 2-$N(CH_3)_2$-Ant and 2-NH_2-Ant show deformation at the C1-position (adjacent site). In the rest of the systems of 1-Sub-Ant and 2-Sub-Ant, out-of-plane deformation of S_1/S_0-MECI occurs at the C9- and C10-positions. The structural deformation of the S_1/S_0-MECI in the 9-Sub-Ant series molecules occurs at the C9-position, with pronounced out-of-plane flipping characteristic of the substituent and the C9-Sub bond. Additionally, the degree of out-of-plane twisting varies significantly among different derivatives. We define three dihedral angles, as depicted in Figure 2. The plane defined by C14−C9−C11, representing the distortion within the anthracene ring plane, is designated as plane α (blue). The plane C14-X-C11, with X being the atom directly connected to C9, is defined as plane β (purple). Plane γ (yellow) is formed by C11−C12−C13-C14, while plane δ (green) is defined by C12−C10−C13. The dihedral angles between these planes are denoted as θ_1 (between α and γ), θ_2 (between β and γ), and θ_3 (between δ and γ), with the corresponding data listed in Table 1. Based on the defined dihedral angles, the S_1/S_0-MECI structures of the 9-Sub-Ant derivatives can be classified into three distinct types: (a) saturated alkyl substituents, characterized by dihedral angles of $\theta_1 \approx 65°$, $\theta_2 \approx 7°$, and $\theta_3 \approx 20°$ (increasing by 10° compared to the S_1/S_0-MECI structure of unsubstituted anthracene); (b) −CHCH2, −$MeSO_2$ substituents, in which plane β is positioned between α and γ, with $\theta_3 > 50°$ (significantly larger than the first type and the unsubstituted anthracene) (note that the C9 and C10 positions are interchanged); (c) other substituents (including the unsubstituted anthracene), exhibiting $\theta_1 \approx 45°$, $\theta_2 \approx 33°$, with the sum of θ_1 and θ_2 approaching 80°, and $\theta_3 < 10°$. The aforementioned three types of structures indicate that at the conical intersection, the anthracene plane is significantly disrupted by pronounced out-of-plane deformations in the central ring. This distortion is inevitably influenced by intermolecular interactions in the solid state, leading to higher relative energies for the S_1/S_0-MECI structures. This forms the

Table 1. Key Dihedral Angles at S_1/S_0-MECI Structures in 9-Sub-Ant

dihedral angle (°)	θ_1	θ_2	θ_3
anthracene	72.99	5.24	10.62
9-BF_2-Ant	49.66	32.05	10.54
9-Br-Ant	67.07	13.05	9.77
9-CF_3-Ant	45.31	37.15	6.86
9-CH_2CH_3-Ant	66.95	6.07	20.73
9-CH_3-Ant	66.92	6.23	21.05
9-$CHCH_2$−Ant	22.91	−2.57	69.84
9-CHCHPyridyl-Ant	0.00	0.00	0.00
9-CHO-Ant	0.00	0.00	0.00
9-Cl-Ant	67.61	10.62	13.50
9-CN-Ant	42.03	41.13	3.40
9-$COCH_3$-Ant	47.76	32.74	6.95
9-COCN-Ant	52.80	24.80	13.45
9-$CONH_2$-Ant	44.96	36.91	5.82
9-COOH-Ant	47.04	33.94	7.31
9-$N(CH_3)_2$-Ant	46.44	28.17	11.31
9-F-Ant	59.38	17.04	10.55
9-$MeSO_2$-Ant	39.00	−13.80	65.52
9-NH_2-Ant	48.70	27.25	7.20
9-NO_2-Ant	45.84	33.05	9.19
9-OCH_3-Ant	52.51	22.82	11.18
9-tBu-Ant	65.21	7.49	20.28
9-Cyclohexyl-Ant	65.82	7.27	20.02

https://doi.org/10.1021/acs.jctc.5c00231
J. Chem. Theory Comput. 2025, 21, 4992−5002

structural basis for designing AIE molecules through the modulation of S_1/S_0-MECI by substituent effects. It is worth mentioning that deformations at nonsubstitution sites are typically driven by C−H bonds, which are less influenced by environmental molecules compared to the overall movement of the substituent group.

Subsequently, we quantitatively elucidate the impact of substituent sites on S_1/S_0-MECI from an energy perspective. We initially investigated the activation free energy ($\Delta G^{\ddagger}$) from S_1 to the S_1/S_0-MECI (Figure 3, Table S2). We employ TST

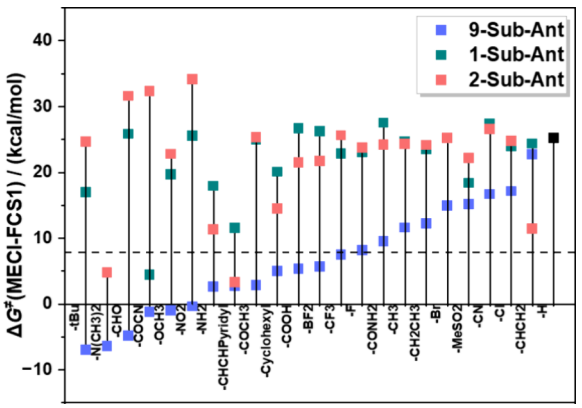

Figure 3. Substituent functional groups and $\Delta G^{\ddagger}$ (MECI-FCS1) in monosubstituted anthracene derivatives.

to quantify the nonradiative decay rate constant through the conical intersection. In Figure 3, the *x*-axis is arranged in ascending order of $\Delta G^{\ddagger}$ values for the 9-Sub-Ant derivatives. Additionally, according to the relationship between k_{nr}^{MECI} and $\Delta G^{\ddagger}$, when $\Delta G^{\ddagger} \leq 7.90$ kcal/mol, $k_{nr}^{MECI} \geq 9.99 \times 10^6$ s^{-1}, which is sufficiently large to significantly influence the photophysical properties of molecules and cannot be neglected. The reference line $\Delta G^{\ddagger} = 7.90$ kcal/mol is shown as a dashed line in Figure 3. The figure reveals that 13 derivatives in the 9-Sub-Ant series have $\Delta G^{\ddagger}$ values below the reference line of 7.90 kcal/mol, while only four systems in 1-Sub-Ant and 2-Sub-Ant have $\Delta G^{\ddagger}$ values below 7.90 kcal/mol, namely 1-N$(CH_3)_2$-Ant, 1-COCN-Ant, 2-N$(CH_3)_2$-Ant, and 2-CHCHPyridyl-Ant. Systems with lower S_1/S_0-MECI relative energies often exhibit structural deformation at the substitution site or adjacent positions. This observation also confirms that S_1/S_0-MECI deformations occurring at substitution sites or adjacent positions effectively reduce the S_1/S_0-MECI relative energy. Combining the S_1/S_0-MECI structural analysis from the previous section with the current findings, the nonradiative decay pathways through the S_1/S_0-MECI are accessible in the single-molecule state for derivatives with $\Delta G^{\ddagger}$ values below 7.90 kcal/mol. In the solid state, large out-of-plane twisting deformations at the C9-Sub or other substituent positions are restricted, leading to an increase in the photoluminescence quantum yield (PLQY) and hence the AIE phenomenon. These observations suggest that 17 monosubstituted anthracene molecules may exhibit AIE properties. Among these derivatives, 9-tBu-Ant possesses the lowest $\Delta G^{\ddagger}$ values. Single substitutions at the C1- and C2-positions marginally alter the S_1/S_0-MECI structure and relative energy and merely benefit

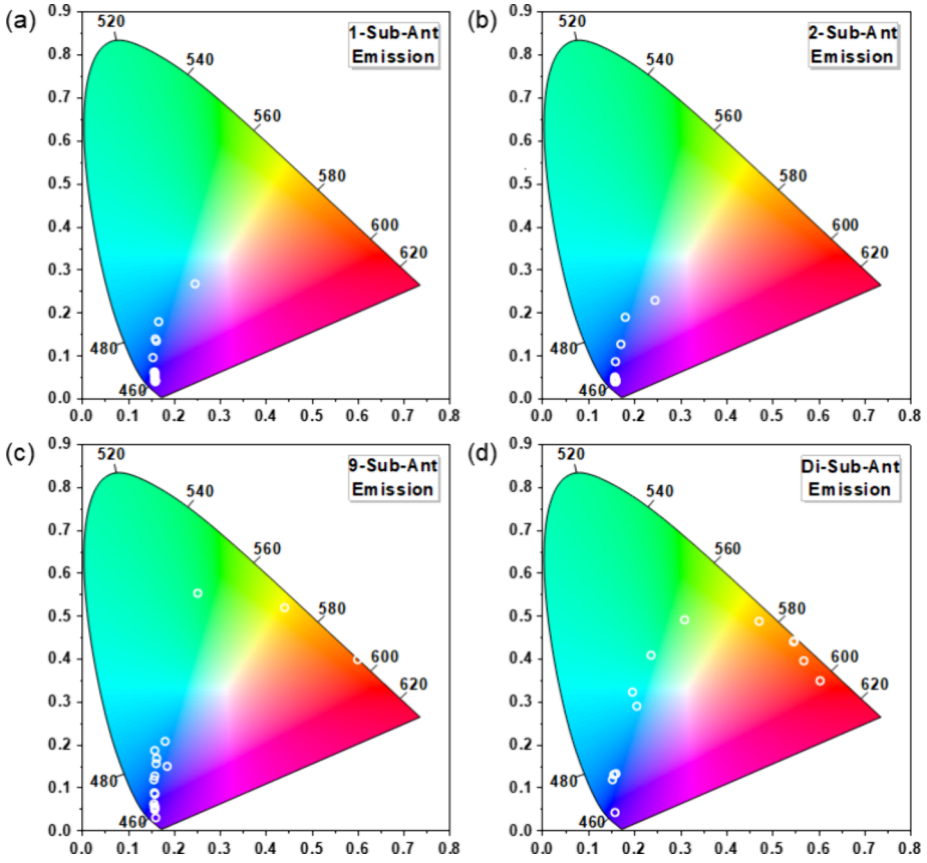

Figure 4. Computational emission CIE coordinates of (a) 1-Sub-Ant; (b) 2-Sub-Ant; (c) 9-Sub-Ant; and (d) Di-Sub-Ant molecules.

https://doi.org/10.1021/acs.jctc.5c00231
J. Chem. Theory Comput. 2025, 21, 4992−5002

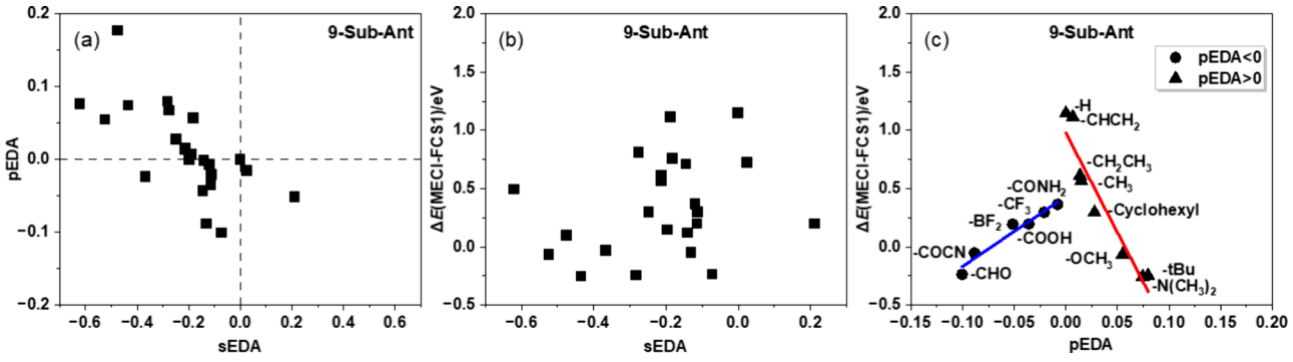

Figure 5. (a) sEDA vs pEDA; (b) sEDA and (c) pEDA vs ΔE(MECI-FCS1); (d) ΔE(MECI-FCS1) = 6.01 (± 0.68) × pEDA + 0.43(±0.04), R^2 = 0.95 (Blue, pEDA < 0), ΔE(MECI-FCS1) = −17.10 (± 2.25) × pEDA + 0.98 (± 0.10), R^2 = 0.91 (red, pEDA > 0).

Table 2. Computational Rate Constants of k_r^{TVCF} and k_{nr}^{TVCF} (Channel I) and k_{nr}^{MECI} (Channel II) and PLQY of AIE Candidates

molecule	k_r^{TVCF} (s^{-1})	k_{nr}^{TVCF} (s^{-1})	$\Delta G^{\ddagger}$ (kcal/mol)	k_{nr}^{MECI} (s^{-1})	PLQY
9-tBu-Ant	3.09×10^{07}	1.87×10^{10}	−7.00	8.41×10^{17}	0.00
9-tBu-Ant (Solid)	2.81×10^{07}	1.90×10^{08}	36.31	1.47×10^{-14}	0.13
9-N$(CH_3)_2$-Ant	1.87×10^{07}	1.82×10^{06}	−6.43	3.20×10^{17}	0.00
9-CHO-Ant	3.21×10^{07}	3.30×10^{03}	−4.82	2.13×10^{16}	0.00
9-COCN-Ant	3.16×10^{07}	1.28×10^{04}	−1.20	4.69×10^{13}	0.00
9-OCH_3-Ant	3.90×10^{07}	3.55×10^{05}	−1.02	3.49×10^{13}	0.00
9-NO_2-Ant	4.32×10^{07}	1.22×10^{04}	−0.36	1.15×10^{13}	0.00
9-NH_2-Ant	3.04×10^{07}	3.27×10^{06}	2.61	7.56×10^{10}	0.00
9-CHCHPyridyl-Ant	4.06×10^{07}	3.03×10^{07}	2.75	5.99×10^{10}	0.00
9-$COCH_3$-Ant	3.44×10^{07}	2.38×10^{06}	2.83	5.21×10^{10}	0.00
9-Cyclohexyl-Ant	4.95×10^{07}	1.35×10^{10}	4.97	1.42×10^{09}	0.00
9-COOH-Ant	4.18×10^{07}	3.02×10^{10}	5.32	7.73×10^{08}	0.00
9-BF_2-Ant	3.21×10^{07}	1.22×10^{09}	5.65	4.47×10^{08}	0.02
9-CF_3-Ant	3.04×10^{07}	1.90×10^{10}	7.48	2.05×10^{07}	0.02
1-N$(CH_3)_2$-Ant	3.92×10^{07}	8.81×10^{03}	4.79	1.94×10^{09}	0.02
1-COCN-Ant	4.49×10^{07}	3.32×10^{04}	4.45	3.38×10^{09}	0.01
2-N$(CH_3)_2$-Ant	2.15×10^{07}	1.75×10^{09}	4.78	1.93×10^{09}	0.01
2-CHCHPyridyl-Ant	7.40×10^{07}	1.03×10^{03}	3.31	2.33×10^{10}	0.00
9,10-N$(CH_3)_2$-Ant	1.72×10^{07}	3.39×10^{07}	−11.23	1.07×10^{21}	0.00
1,4-N$(CH_3)_2$-Ant	4.94×10^{05}	2.38×10^{10}	−7.71	2.80×10^{18}	0.00
2,9-N$(CH_3)_2$-Ant	2.14×10^{07}	2.17×10^{10}	−4.41	1.06×10^{16}	0.00
1,9-N$(CH_3)_2$-Ant	NA	NA	−4.33	9.23×10^{15}	NA
2,10-N$(CH_3)_2$-Ant	2.39×10^{07}	1.45×10^{10}	−2.86	7.73×10^{14}	0.00
2,3-N$(CH_3)_2$-Ant	1.88×10^{07}	7.14×10^{04}	2.22	1.46×10^{11}	0.00
2,7-N$(CH_3)_2$-Ant	5.02×10^{05}	7.62×10^{04}	7.43	2.20×10^{07}	0.02

the AIE effect. Therefore, monosubstitution at the C9-position has a higher probability of yielding AIE molecules.

We further simulate the absorption and fluorescence spectra of monosubstituted anthracene derivatives. For comparative purposes, the simulated fluorescence emission spectra peak values are plotted into CIE (Commission Internationale de l'Eclairage) chromaticity coordinates in Figure 4. Results indicate that 1-Sub-Ant systems primarily exhibit deep blue emission, with minimal impact from changes in the substituent functional group on fluorescence emission color. Following the 1-Sub-Ant systems, the 2-Sub-Ant systems exhibit slightly more pronounced color modulation. In contrast, the 9-Sub-Ant systems demonstrate the most significant color modulation. Overall, in terms of both fluorescence color modulation and S_1/S_0-MECI structural and relative energy modulation, single substitutions at the C9-position exhibit higher sensitivity compared to those at the C1- and C2-positions. This heightened sensitivity results in a higher success rate for screening AIE molecules within the 9-Sub-Ant series. Conversely, when the goal is to introduce functional groups without significantly impacting single-molecule emission performance, such as color and fluorescence efficiency relative to anthracene, substitutions at the C1- and C2-positions are preferred.

3.2. Substituent Functional Groups vs S_1/S_0-MECI. We now explore the effect of various substituent functional groups (with electron-donating or electron-withdrawing character) on the S_1/S_0-MECI relative energy of 9-Sub-Ant.

We employ the sEDA/pEDA descriptors to evaluate the σ and π electron-donating and electron-withdrawing abilities of the substituents, with the data presented in Table S3. The correlation between sEDA/pEDA descriptors and the relative energy ΔE(MECI-FCS1) for the 9-Sub-Ant series is illustrated in Figure 5. The sEDA/pEDA correlation plot in Figure 5a highlights the diversity of substituents selected in this study. The selection of these substituents is made based on ref 47, and such selection guarantees distinguishable sEDA/pEDA values for systems with different substituents. Among these

https://doi.org/10.1021/acs.jctc.5c00231
J. Chem. Theory Comput. 2025, 21, 4992−5002

substituents, $-BF_2$ and $-MeSO_2$ function as σ-donors, whereas the remaining substituents act as σ-acceptors. Figure 5b demonstrates that sEDA exhibits no significant linear correlation with ΔE(MECI-FCS1), indicating that the σ electron-donating or electron-withdrawing abilities of the substituents have minimal influence on ΔE(MECI-FCS1). Contrarily, pEDA exhibits a noticeable linear trend, where a larger absolute pEDA value corresponds to a smaller ΔE(MECI-FCS1). This suggests that stronger π-electron-donating or electron-withdrawing abilities lead to lower S_1/S_0-MECI relative energies. We further analyze the relationship between substituent functional groups and ΔE(MECI-FCS1) with selected π-accepting and π-donating groups (details in Figure S2), as shown in Figure 5c. For π-donors (pEDA > 0), the linear regression equation is ΔE(MECI-FCS1) = $-17.10(\pm 2.25) \times$ pEDA + $0.98(\pm 0.10)$, with a coefficient of determination (R^2) of 0.91, indicating a strong linear relationship. For π-acceptors (pEDA < 0), the linear regression equation is ΔE(MECI-FCS1) = $6.01(\pm 0.68) \times$ pEDA + $0.43(\pm 0.04)$, with $R^2 = 0.95$. Comparison of the slopes of the fitted curves reveals that π-donors exert a more pronounced influence on modulating ΔE(MECI-FCS1) than π-acceptors, which indicates that single substitution at the C9-position with electron-donating groups results in lower S_1/S_0-MECI relative energies in anthracene derivatives. This modulation is crucial for designing AIE molecules as it directly influences the photophysical properties, including PLQY and emission behavior. Based on these findings, the influence of substituent functional groups on the photophysical microprocesses of the 9-Sub-Ant system is systematically investigated, providing a quantitative assessment of the S_1 state decay rate constants for each process. These data are presented in Table 2 and Table S4. As shown in Table 2, the k_{nr}^{MECI}values for these systems are significantly larger than the k_{nr}^{TVCF}, which directly results in the PLQY of these systems approaching zero in the single-molecule state. In the solid state, the deformation of the S_1/S_0-MECI is influenced by intermolecular interactions, which elevate the S_1/S_0-MECI relative energy and restrict its accessibility. This limitation reduces nonradiative decay through channel II, thereby increasing the PLQY and enhancing the solid-state emission.

Furthermore, we investigate the impact of substituent functional groups on the fluorescence emission color of the 9-Sub-Ant derivatives. The vertical excitation energies and simulated corresponding absorption and emission spectra are shown in Table 3 and Figure S1. Table 3 also presents the reorganization energies based on the S_0 potential energy surface. Compared with unsubstituted anthracene, all 9-Sub-Ant derivatives display red-shifted absorption energies. The most significant red shift is observed in 9-COCN-Ant, with an absorption peak at 392 nm, representing a 53 nm red shift relative to that of anthracene. Substantial red shifts are also noted for the −CHCHPyridyl, −CHO, $-NH_2$, and −tBu groups, with absorption peaks ranging from 370 to 390 nm. In contrast, the absorption peaks of other derivatives are clustered around 355 nm, corresponding to only a 16 nm red shift from anthracene. This suggests that the absorption energies of most 9-Sub-Ant derivatives remain largely unchanged with varying substituents. Regarding vertical emission energies, 9-CHCHPyridyl-Ant exhibits the largest red shift, with an emission peak at 499 nm, a shift of 102 nm from that of anthracene. As for emission, substituents that cause notable red shifts include −CHO, $-COCH_3$, −COCN, $-N(CH_3)_2$, $-NH_2$, and −tBu, with emission peaks ranging from 440 to 459 nm. These substituents closely correspond to those that exhibit significant red shifts in absorption relative to that of anthracene. The emission peaks of the other 9-Sub-Ant derivatives are primarily around 415 nm, which is a 17 nm red shift from anthracene. This alignment with the absorption peak red shifts, indicating that the Stokes shifts are similar to those of anthracene, at approximately 60 nm. The discussion suggests that the reorganization energy for most 9-Sub-Ant derivatives should align closely with those of anthracene. To confirm this, we compute the reorganization energies using both the harmonic oscillator approximation and the four-point method. It can be seen in Table 3 that for most cases, the results from these two methods are consistent, although the harmonic oscillator approximation results are slightly overestimated for some flexible systems. Overall, the reorganization energies of most 9-Sub-Ant derivatives are comparable to that of anthracene, with values of around 2300 cm^{-1} (as shown in Table 3). Notably, higher reorganization energies are observed for 9-CHCHPyridyl-Ant, 9-$COCH_3$-Ant, 9-$N(CH_3)_2$-Ant, and 9-tBu-Ant, all exceeding 3000 cm^{-1}. These values align with the systems previously identified for significant red shifts in both absorption and emission energies relative to those of anthracene.

Table 3. Computational Vertical Excitation Energies at S_0 and S_1 Optimized Geometries and the Reorganization Energies of 9-Sub-Ant

molecule	absorption (nm)	emission (nm)	reorganization energy (cm^{-1})	
			harmonic oscillator approximation	four-point method
Anthracene	339	397	2239.98	2184.79
9-BF_2-Ant	353	415	2277.31	2163.99
9-Br-Ant	354	416	2135.03	2131.99
9-CF_3-Ant	347	415	2630.36	2426.69
9-CH_2CH_3-Ant	352	410	2165.82	2165.47
9-CH_3-Ant	350	409	2170.68	2147.24
9-$CHCH_2$−Ant	355	429	2382.45	2415.67
9-CHCHPyridyl-Ant	370	499	5582.24	3995.34
9-CHO-Ant	373	442	2228.45	2234.91
9-Cl-Ant	352	411	2160.91	2137.01
9-CN-Ant	361	419	2015.03	2005.8
9-$COCH_3$-Ant	347	437	5089.88	3210.07
9-COCN-Ant	392	459	1993.91	1933.99
9-$CONH_2$-Ant	349	414	2515.99	2479.22
9-COOH-Ant	352	424	2820.52	2585.27
9-$N(CH_3)_2$-Ant	351	448	5130.87	2175.52
9-F-Ant	353	416	1753.16	2212.67
9-$MeSO_2$-Ant	359	426	2444.08	2464.93
9-NH_2-Ant	379	451	2272.91	2200.25
9-NO_2-Ant	361	425	2075.00	2073.54
9-OCH_3-Ant	349	412	2258.38	2206.91
9-tBu-Ant	367	454	3008.88	3032.54
9-Cyclohexyl-Ant	355	416	2382.47	2431.16

3.3. From Monosubstitution to Disubstitution. To systematically elucidate the differences in emission performance between singly and doubly substituted anthracene derivatives, we employed the $-N(CH_3)_2$ group for double substitution and explored all 15 possible double substitution

https://doi.org/10.1021/acs.jctc.5c00231
J. Chem. Theory Comput. 2025, 21, 4992−5002

configurations on the anthracene ring (chemical structures are shown in Scheme 1).

We first examine the fluorescence color distribution of the Di-Sub-Ant systems. Unlike their singly substituted counterparts, which typically exhibit blue fluorescence, the doubly substituted derivatives display a significantly broader fluorescence color range (Figure 4d), including not only deep blue but also green and orange regions. The vertical excitation energies and reorganization energies are summarized in Table S4. In general, doubly substituted anthracene derivatives exhibit a slight red shift in absorption and emission energies compared to singly substituted derivatives. The red shifts are caused by the conformational changes of the additional $-N(CH_3)_2$ group, which is consistent with the increasing trend in reorganization energies. This finding is also in agreement with the experimental observations.[53]

We then optimized the S_1/S_0-MECI structures of the doubly substituted anthracene derivatives (Figure 6a). Among the 15

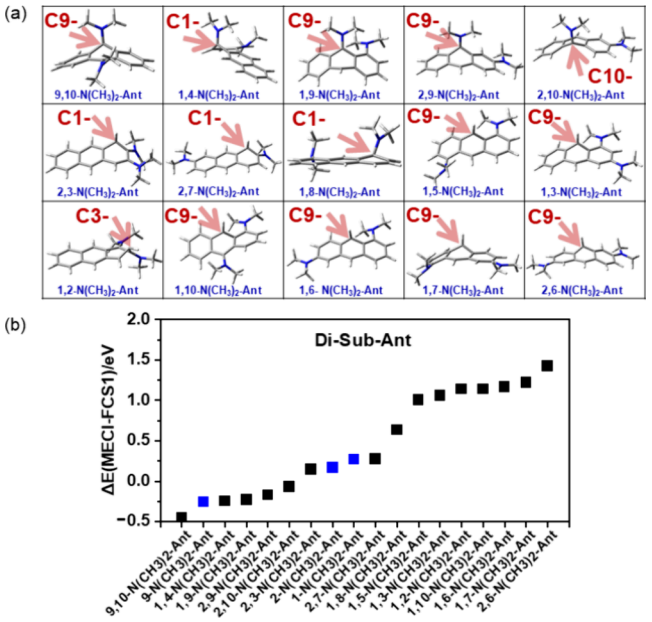

Figure 6. Optimized S_1/S_0-MECI relative energies and structures of Di-Sub-Ant.

derivatives, 1,4-$N(CH_3)_2$-Ant, 2,3-$N(CH_3)_2$-Ant, 2,7-$N(CH_3)_2$-Ant and 1,8-$N(CH_3)_2$-Ant exhibited S_1/S_0-MECI structural deformation at the C1-position, 1,2-$N(CH_3)_2$-Ant deformation occurred at the C3-position, and the remaining 10 molecules at the C9- or C10-position. Additionally, six Di-Sub-Ant systems exist with significant out-of-plane twisting at the substitution sites in the S_1/S_0-MECI geometry. As shown in Figure 6b, double substitution on equivalent carbons within the same ring of anthracene results in lower S_1/S_0-MECI relative energy compared to single substitution; they exhibit consistent deformation characteristics as well (Figure 6). For example, 9,10-$N(CH_3)_2$-Ant exhibit lower relative energy (ΔE(MECI-FCS1)) than 9-$N(CH_3)_2$-Ant, and same trend is observed for 1,4-$N(CH_3)_2$-Ant and 1-$N(CH_3)_2$-Ant, as well as for 2,3-$N(CH_3)_2$-Ant and 2-$N(CH_3)_2$-Ant. We further quantitatively investigated the photophysical properties of the doubly substituted anthracene derivatives. As listed in Table 2, seven Di-Sub-Ant exhibit $\Delta G^{\ddagger}$ values below 7.90 kcal/mol, indicating non-negligible nonradiative decay via the S_1/S_0-MECI in approximately half of the doubly substituted anthracene derivatives and thus can be identified as potential AIE candidates.

3.4. Validation of the Design Strategy for AIEgens.

The filtered-out candidate AIE molecules are listed in Figure 7a. These candidates exhibit low S_1/S_0-MECI (Cartesian coordinates are listed in the Supporting Information) in the gaseous phase, making them energetically more inclined to quench emission or result in weak emission via the S_1/S_0-MECI pathway. Structurally, the S_1/S_0-MECI deformation in these systems is predominantly localized at the substitution sites. In the solid state, intermolecular interactions significantly influence the out-of-plane structural deformations, thereby inevitably increasing the relative energy of the S_1/S_0-MECI. This energetic shift restricts nonradiative decay via the S_1/S_0-MECI (channel II), thereby enhancing PLQY. Notably, 9-CHO-Ant,[54] 9-CHCHPyridyl-Ant,[55] and 9,10-$N(CH_3)_2$-Ant[56] have been previously reported as AIE systems. These findings validate the efficacy of our strategy in identifying AIE-active molecules by modulating the structures and relative energies of the S_1/S_0-MECI through a substituent effect.

Herein, we select 9-tBu-Ant as an example, which has not been reported as an AIE molecule, to further validate our protocol. We quantitatively calculate its solid-state photophysical processes. The crystal structure of this molecule (ID 1126440) was obtained from the Cambridge Crystallographic Data Centre (CCDC) and used as the basis for constructing a 3 × 3 × 3 supercell for solid-state computations. The optimized structures of S_1/S_0-MECI in the solid state are depicted in Figure 7c, with the corresponding relative energies and rate constants summarized in Table 2. In the solid state, the S_1/S_0-MECI structure of 9-tBu-Ant closely resembles that of the single-molecule state, with significant out-of-plane torsion of the C9-substituent bond characterized by dihedral angles of θ_1 = 64.82°, θ_2 = 7.68°, and θ_3 = 21.15°. These dihedral angles remain nearly unchanged in the solid state compared with the single-molecule state. The vertical excitation energies for the S_0-min and S_1-min structures are 366 and 458 nm, respectively, exhibiting minimal deviation from those in the single-molecule state. The $\Delta G^{\ddagger}$ value is 36.31 kcal/mol, significantly higher than the monomeric value of (∼−7.00 kcal/mol) and also much higher than the reference value of 7.90 kcal/mol. This elevated $\Delta G^{\ddagger}$ value results in a near-zero nonradiative decay rate via the S_1/S_0-MECI pathway. The reorganization energy of 2881.53 cm^{-1} is lower than that in the single-molecule state. The decay rate constant k_r^{TVCF} and nonradiative decay rate constant k_{nr}^{TVCF} in the solid phase are 2.81 × 10^7 and 1.90 × 10^8 s^{-1}, respectively. With the corresponding PLQY estimated to be 12.9%, much higher than the near-zero PLQY in the single-molecule state. Although the k_{nr}^{TVCF} in the solid state is also reduced, its magnitude is far less than that of k_{nr}^{MECI}. Therefore, the enhancement of PLQY in 9-tBu-Ant is primarily governed by the reduced nonradiative decay rate via channel II. This example demonstrates the validity of our proposed design strategy for AIE molecules by modulating the S_1/S_0-MECI structures and relative energies through the substituent effect.

4. CONCLUSIONS

By employing anthracene derivatives as carriers, this study has systematically investigated the regulatory patterns of substituent functional groups, positions, and quantities on the relative energy and structural deformation of the S_1/S_0-MECI.

https://doi.org/10.1021/acs.jctc.5c00231
J. Chem. Theory Comput. 2025, 21, 4992−5002

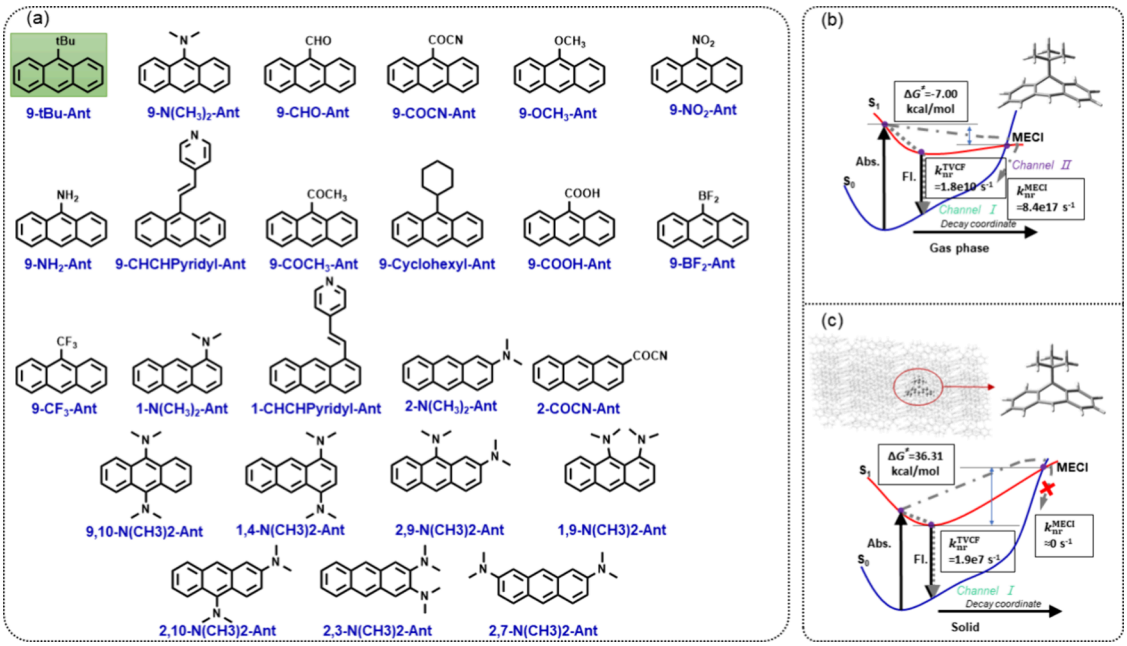

Figure 7. (a) Chemical structures of AIE candidates and the schematic graph of the two nonradiative decay channels for 9-tBu-Ant (b) in the gas phase; (c) in the solid phase.

By modulating the properties of the MECI through these changes, we effectively regulated the photophysical properties. Through quantitative calculations, we have identified a series of single molecules exhibiting low S_1/S_0-MECI energies and significant MECI structural deformation. Furthermore, 24 AIEgens have been identified as candidates from a pool of 81 anthracene derivatives.

In the monosubstituted molecules, most S_1/S_0-MECI structural deformation predominantly occurs in the central ring, resembling a paper crane with significant out-of-plane twisting at the C9-X position. This large out-of-plane twisting is restricted in the solid phase, thereby increasing the MECI relative energy, limiting nonradiative decay via channel II, and enhancing PLQY. As for the energy perspective, only four systems exhibit $\Delta G^{\ddagger}$ values below 7.90 kcal/mol in 1-Sub-Ant and 2-Sub-Ant, while 13 molecules exhibit in 9-Sub-Ant. This suggests that substitution at the C9-position of anthracene is favorable for the design of AIEgens, while those at C1- and C2-positions are not beneficial to the AIE effect. In 9-Sub-Ant systems, substituents with stronger π-electron-donating or electron-withdrawing capabilities generally result in lower S_1/S_0-MECI relative energies, with electron-donating groups exhibiting a more pronounced modulation effect, leading to a potentially more remarkable AIE effect. Double substitution may further regulate the S_1/S_0-MECI relative energy compared to single substitution, which may further enhance the AIE effect. Additionally, double substitutions can significantly modulate emission color. We performed solid-state quantitative calculations on 9-tBu-Ant, which has not been reported as an AIE molecule before, confirming its AIE nature and validating our design strategy. In summary, we provide a systematic approach to designing AIE molecules by modulating the S_1/S_0-MECI through the substituent effect.

■ ASSOCIATED CONTENT

Supporting Information

The Supporting Information is available free of charge at https://pubs.acs.org/doi/10.1021/acs.jctc.5c00231.

Computational details including geometry optimization and vertical excitation energy calculation, minimum energy conical intersection (MECI) calculation, sEDA/pEDA, unique S_1/S_0-MECI structure, criteria for substituent selection, the ω value corresponding to the ω-B97XD functional in different systems, computational rate constants of k_r^{TVCF} and k_{nr}^{TVCF} (channel I) and k_{nr}^{MECI} (channel II) of target anthracene derivatives, sEDA/pEDA and ΔE (MECI-FCS1) of monosubstituted anthracene derivatives, computational vertical excitation energies at S_0 and S_1 optimized geometries and the reorganization energies of 1-Sub-Ant, 2-Sub-Ant and Di-Sub-Ant, absorption and emission spectra of target molecule, relationship between substituent functional groups and ΔE(MECI-FCS1) with selected π-accepting and π-donating groups with the excluded points, and Cartesian coordinates of optimized S_1/S_0-MECI structures for AIE candidates (PDF)

■ AUTHOR INFORMATION

Corresponding Authors

Qi Ou − *Sinopec Research Institute of Petroleum Processing Co., Beijing 100083, P. R. China*; Email: ouqi.ripp@sinopec.com

Zhigang Shuai − *Department of Chemistry, MOE Key Laboratory of Organic OptoElectronics and Molecular Engineering, Tsinghua University, Beijing 100084, P. R. China; School of Science and Engineering, The Chinese University of Hong Kong, Shenzhen, Guangdong 518172, P. R. China*; orcid.org/0000-0003-3867-2331; Email: shuaizhigang@cuhk.edu.cn

https://doi.org/10.1021/acs.jctc.5c00231
J. Chem. Theory Comput. 2025, 21, 4992−5002

Author

Ping-An Yin − *Department of Chemistry, MOE Key Laboratory of Organic OptoElectronics and Molecular Engineering, Tsinghua University, Beijing 100084, P. R. China*

Complete contact information is available at: https://pubs.acs.org/10.1021/acs.jctc.5c00231

Author Contributions

The manuscript was written through contributions of all authors. All authors have given approval to the final version of the manuscript.

Notes

The authors declare no competing financial interest.

■ ACKNOWLEDGMENTS

This work is supported by the National Natural Science Foundation of China (grant nos. T2350009 and 22433007) and the Guangdong Provincial Natural Science Foundation grant no. 2024A1515011185, as well as Shenzhen city Peacock Team Project KQTD20240729102028801. Q.O. acknowledges financial support from China Petroleum & Chemical Corp (funding number 124014).

■ REFERENCES

(1) Luo, J.; Xie, Z.; Lam, J. W. Y.; Cheng, L.; Chen, H.; Qiu, C.; Kwok, H. S.; Zhan, X.; Liu, Y.; Zhu, D.; et al. Aggregation-induced emission of 1-methyl-1,2,3,4,5-pentaphenylsilole. *Chem. Commun.* **2001**, 1740−1741.

(2) Tong, H.; Hong, Y. N.; Dong, Y. Q.; Häussler, M.; Lam, J. W. Y.; Li, Z.; Guo, Z. F.; Guo, Z. H.; Tang, B. Z. Fluorescent "light-up" bioprobes based on tetraphenylethylene derivatives with aggregation-induced emission characteristics. *Chem. Commun.* **2006**, 3705−3707.

(3) Chen, M.; Li, L. Z.; Nie, H.; Tong, J. Q.; Yan, L. L.; Xu, B.; Sun, J. Z.; Tian, W. J.; Zhao, Z. J.; Qin, A. J.; et al. Tetraphenylpyrazine-based AIEgens: facile preparation and tunable light emission. *Chem. Sci.* **2015**, *6*, 1932−1937.

(4) You, Y.; Tang, C.; Lin, S.; Zeng, D.; Cong, Y.; Wang, D.; Chen, X. Photoactivatable aggregation-induced emission luminogens based on photodehydrogenation reactions for biomedical applications. *Luminescence* **2024**, *39*, No. e4645.

(5) Zhou, Y.; Li, D.; Yue, X.; Shi, Y.; Li, C.; Wang, Y.; Chen, Y.; Liu, Q.; Ding, D.; Wang, D.; Shen, J.; et al. Enhancing Root Canal Therapy with NIR-II Semiconducting Polymer AIEgen and Low-Concentration Sodium Hypochlorite Synergy. *Adv. Healthcare Mater.* **2024**, *13*, 2401434.

(6) Deng, L.-l.; Huang, X.-l.; Liu, S.-m.; Yang, Y.-p.; He, H.-f.; Fu, L.; Chen, H.-y.; Zhao, F.; Xia, H.-y.; Xiong, Z.-h. AIE-active N-heterocyclic carbene Cu(I) complexes: Stimuli-responsive with hypsochromic or bathochromic mechanochromic phosphorescence through switchable C−H···F interactions. *Dyes Pigm.* **2024**, *230*, No. 112346.

(7) Barman, D.; Barman, D.; Bhattacharyya, K.; Iyer, P. K. Engineering Single Component Luminogens to Multicomponent Charge-transfer Co-crystal Substrate as New Frontiers for Sensitive SERS Detection. *Adv. Opt. Mater.* **2024**, *12*, 2401352.

(8) Zeng, J. J.; Guo, J. J.; Liu, H.; Lam, J. W. Y.; Zhao, Z. J.; Chen, S. M.; Tang, B. Z. Aggregation-Induced Delayed Fluorescence Luminogens for Efficient Organic Light-Emitting Diodes. *Chem-asian J.* **2019**, *14*, 828−835.

(9) Itsoponpan, T.; Wongkaew, P.; Prakanpo, N.; Sukthawee, T.; Suyoadsuk, T.; Promarak, V. Deep Blue Emitter with a Combination of Hybridized Local and Charge Transfer Excited State and Aggregation-Induced Emission Features for Efficient Non-Doped OLED. *ChemPlusChem.* **2024**, *89*, No. e202400438.

(10) Petdee, S.; Chantanop, N.; Arunlimsawat, S.; Saenubol, A.; Nalaoh, P.; Sudyoadsuk, T.; Promarak, V. Excited-state intramolecular proton-transfer solid-state fluorophores with aggregation-induced emission as efficient emitters for electroluminescent devices. *CrystEngComm* **2024**, *26*, 4698−4707.

(11) Zhang, L.; Wang, L.; Samedov, K.; Chen, M.; Chen, D.; Cai, Y. High-Lying Triplet Excitons Utilization of Silole Derivatives Enables their Efficiency Breakthrough in OLEDs. *Adv. Funct. Mater.* **2024**, *34*, 2410250.

(12) Mohammed Hashim, K. K.; Manoj, E. Aminoguanidine-based bioactive proligand as AIEE probe for anticancer and anticovid studies. *RSC Adv.* **2024**, *14*, 13654−13668.

(13) Xue, K.; Zhao, Y.; Sun, S.; Li, Y.; Qi, Z. A near-infrared aggregation-induced emission photosensitizer targeting mitochondria for depleting Cu2+ to trigger light-activated cancer cells oncosis. *Bioorg. Chem.* **2024**, *143*, No. 107020.

(14) Bu, W.; Guo, X.; Lv, X.; Zhang, Q.; Zuo, H.; Wu, Q.; Wu, H.; Yu, C.; Jiao, L.; Hao, E. Rational design of a two-photon probe with solvatochromic emission and AIE-activity for lipid droplet specific imaging. *Dyes Pigm.* **2023**, *220*, No. 111735.

(15) You, Y.; Tang, C.; Lin, S.; Zeng, D.; Cong, Y.; Wang, D.; Chen, X. Photoactivatable aggregation-induced emission luminogens based on photodehydrogenation reactions for biomedical applications. *Luminescence* **2024**, *39*, No. e4645.

(16) Wang, Y. Y.; Yu, X. H.; Huang, Z. H.; Peng, J. F.; Zhou, L. J.; Cai, L. T.; Zhao, X. X.; Zhang, P. F. Berberine-doped montmorillonite nanosheet for photoenhanced antibacterial therapy and wound healing. *J. Colloid Interface Sci.* **2024**, *676*, 774−782.

(17) Wang, C.; Li, S.; Qian, B.; Sun, J.; He, Z.; Wang, Y.; Zhang, S.; Luo, C. AIEgen-functionalized nanoprobes and nanomedicines for cancer diagnosis and therapy. *Coord. Chem. Rev.* **2024**, *520*, No. 216148.

(18) Liu, J.; Ou, X.; Wang, K.; Wang, K.; Gui, L.; Song, F.; Chen, C.; Lam, J. W. Y.; Yuan, Z.; Tang, B. Z. Two-Photon-Activated Heavy-Atom Free AIEgen for Highly Efficient Type I Photodynamic Therapy. *Adv. Funct. Mater.* **2024**, *34*, 2410202.

(19) Dai, D.; Yang, J.; Wang, Y.; Yang, Y. Recent Progress in Functional Materials for Selective Detection and Removal of Mercury(II) Ions. *Adv. Funct. Mater.* **2021**, *31*, 2006168.

(20) Sun, J.; Li, H.; Li, Y.; Wang, Y.; Wang, S.; Pan, M. Fluorescence probe based on ZIF-8-constrained AuNCs aggregation-induced enhancement applying for specific Cu^{2+} detection in water and fish samples. *J. Food Compos. Anal.* **2024**, *135*, No. 106591.

(21) Hazarika, S.; Ilango, B.; Parthasarathy, V.; Velusamy, M.; Kathiravan, A. Tetraphenylethylene tethered 1-(pyridine-2-yl)-imidazo[1,5-*a*]pyridine: Synthesis, aggregation induced emission, copper(II) ion detection and imaging of latent fingerprint. *Dyes Pigm.* **2024**, *231*, No. 112387.

(22) Zuo, Y.; Kwok, R. T. K.; Sun, J.; Lam, J. W. Y.; Tang, B. Z. Aggregation-induced emission luminogens for super-resolution imaging. *Chem. Phys. Rev.* **2024**, *5*, No. 011309.

(23) Lu, H.; Wang, K.; Liu, B.; Wang, M.; Huang, M.; Zhang, Y.; Yang, J. Rational design of systematic AIEEgens further modified by substituents from a novel chain structure. *Sci. China Chem.* **2021**, *64*, 52−60.

(24) Zhang, J. N.; Kang, H.; Li, N.; Zhou, S. M.; Sun, H. M.; Yin, S. W.; Zhao, N.; Tang, B. Z. Organic solid fluorophores regulated by subtle structure modification: color-tunable and aggregation-induced emission. *Chem. Sci.* **2017**, *8*, 577−582.

(25) Yang, G.; Xue, Z.-M.; Liang, L.; Meng, F.; Liu, K.-Y.; Wang, J.-H.; Lin, H.-T.; Zhao, W.-X.; Chen, S.-H.; Yamato, T.; et al. Substituent effects on the mechanochromic behaviour of pyrene-based AIEgens. *J. Photochem. Photobiol., A* **2025**, *459*, No. 116020.

(26) Long, X.; Wu, J.; Yang, S.; Deng, Z.; Zheng, Y.; Zhang, W.; Jiang, X.-F.; Lu, F.; Li, M.-D.; Xu, L. Discovery of and insights into one-photon and two-photon excited ACQ-to-AIE conversion via positional isomerization. *J. Mater. Chem. C* **2021**, *9*, 11679−11689.

(27) Zuo, Y.; Liu, J.; Li, P.; Li, K.; Lam, J. W. Y.; Wu, D.; Tang, B. Z. Full-color-tunable AIE luminogens for 4D code, security patterns, and multicolor LEDs. *Cell Rep. Phys. Sci.* **2023**, *4*, No. 101202.
(28) Shen, X. Y.; Wang, Y. J.; Zhang, H.; Qin, A.; Sun, J. Z.; Tang, B. Z. Conjugates of tetraphenylethene and diketopyrrolopyrrole: tuning the emission properties with phenyl bridges. *Chem. Commun.* **2014**, *50*, 8747−8750.
(29) Zhao, W.; He, Z.; Peng, Q.; Lam, J. W. Y.; Ma, H.; Qiu, Z.; Chen, Y.; Zhao, Z.; Shuai, Z.; Dong, Y.; Tang, B. Z.; et al. Highly sensitive switching of solid-state luminescence by controlling intersystem crossing. *Nat. Commun.* **2018**, *9*, 3044.
(30) Tseng, N.-W.; Liu, J.; Ng, J. C. Y.; Lam, J. W. Y.; Sung, H. H. Y.; Williams, I. D.; Tang, B. Z. Deciphering mechanism of aggregation-induced emission (AIE): Is E−Zisomerisation involved in an AIE process? *Chem. Sci.* **2012**, *3*, 493−497.
(31) Mei, J.; Hong, Y. N.; Lam, J. W. Y.; Qin, A. J.; Tang, Y. H.; Tang, B. Z. Aggregation-Induced Emission: The Whole Is More Brilliant than the Parts. *Adv. Mater.* **2014**, *26*, 5429−5479.
(32) Peng, Z.; Ji, Y.; Huang, Z.; Tong, B.; Shi, J.; Dong, Y. A strategy for the molecular design of aggregation-induced emission units further modified by substituents. *Mater. Chem. Front* **2018**, *2*, 1175−1183.
(33) Zhao, G. N.; Tang, B.; Dong, Y. Q.; Xie, W. H.; Tang, B. Z. A unique fluorescence response of hexaphenylsilole to methyl parathion hydrolase: a new signal generating system for the enzyme label. *J. Mater. Chem. B* **2014**, *2*, 5093−5099.
(34) Xue, S.; Meng, L.; Wen, R.; Shi, L.; Lam, J. W.; Tang, Z.; Li, B. S.; Tang, B. Z. Unexpected aggregation induced circular dichroism, circular polarized luminescence and helical assembly from achiral hexaphenylsilole (HPS). *RSC Adv.* **2017**, *7*, 24841−24847.
(35) Zhang, J.; Ma, S.; Fang, H.; Xu, B.; Sun, H.; Chan, I.; Tian, W. Insights into the origin of aggregation enhanced emission of 9,10-distyrylanthracene derivatives. *Mater. Chem. Front* **2017**, *1*, 1422−1429.
(36) Chen, J.; Ma, S.; Zhang, J.; Li, B.; Xu, B.; Tian, W. Low-Loss Optical Waveguide and Highly Polarized Emission in a Uniaxially Oriented Molecular Crystal Based on 9,10-Distyrylanthracene Derivatives. *ACS Photonics* **2015**, *2*, 313−318.
(37) Li, W.; Chen, D.; Wang, H.; Luo, S.; Dong, L.; Zhang, Y.; Shi, J.; Tong, B.; Dong, Y. Quantitation of Albumin in Serum Using "Turn-on" Fluorescent Probe with Aggregation-Enhanced Emission Characteristics. *ACS Appl. Mater. Interfaces* **2015**, *7*, 26094−26100.
(38) Ou, Q.; Peng, Q.; Shuai, Z. G. Toward Quantitative Prediction of Fluorescence Quantum Efficiency by Combining Direct Vibrational Conversion and Surface Crossing: BODIPYs as an Example. *J. Phys. Chem. Lett.* **2020**, *11*, 7790−7797.
(39) Li, Q. S.; Blancafort, L. A conical intersection model to explain aggregation induced emission in diphenyl dibenzofulvene. *Chem. Commun.* **2013**, *49*, 5966−5968.
(40) Yin, P.; Ou, Q.; Peng, Q.; Shuai, Z. Substituent-controlled aggregate luminescence: Computational unraveling of S1/S0 surface crossing. *Aggregate* **2023**, *4*, No. e291.
(41) Shao, Y.; Head-Gordon, M.; Krylov, A. I. The spin−flip approach within time-dependent density functional theory: Theory and applications to diradicals. *J. Chem. Phys.* **2003**, *118*, 4807−4818.
(42) Bernard, Y. A.; Shao, Y.; Krylov, A. I. General formulation of spin-flip time-dependent density functional theory using non-collinear kernels: Theory, implementation, and benchmarks. *J. Chem. Phys.* **2012**, *136*, No. 204103.
(43) Chai, J.-D.; Head-Gordon, M. Long-range corrected hybrid density functionals with damped atom−atom dispersion corrections. *Phys. Chem. Chem. Phys.* **2008**, *10*, 6615−6620.
(44) Shao, Y.; Gan, Z.; Epifanovsky, E.; Gilbert, A. T. B.; Wormit, M.; Kussmann, J.; Lange, A. W.; Behn, A.; Deng, J.; Feng, X.; et al. Advances in molecular quantum chemistry contained in the Q-Chem 4 program package. *Mol. Phys.* **2015**, *113*, 184−215.
(45) Shuai, Z.; Peng, Q. Organic light-emitting diodes: theoretical understanding of highly efficient materials and development of computational methodology. *Natl. Sci. Rev.* **2017**, *4*, 224−239.
(46) Niu, Y.; Li, W.; Peng, Q.; Geng, H.; Yi, Y.; Wang, L.; Nan, G.; Wang, D.; Shuai, Z. MOlecular MAterials Property Prediction Package (MOMAP) 1.0: a software package for predicting the luminescent properties and mobility of organic functional materials. *Mol. Phys.* **2018**, *116*, 1078−1090.
(47) Oziminski, W. P.; Dobrowolski, J. C. σ- and π-electron contributions to the substituent effect: natural population analysis. *J. Phys. Org. Chem.* **2009**, *22*, 769−778.
(48) Dobrowolski, J. C.; Lipiński, P. F. J.; Karpińska, G. Substituent Effect in the First Excited Singlet State of Monosubstituted Benzenes. *J. Phys. Chem. A* **2018**, *122*, 4609−4621.
(49) Frisch, M. J.; Trucks, G. W.; Schlegel, H. B.; Scuseria, G. E.; Robb, M. A.; Cheeseman, J. R.; Scalmani, G.; Barone, V.; Petersson, G. A.; Nakatsuji, H.; Li, X.; Caricato, M.; Marenich, A. V.; Bloino, J.; Janesko, B. G.; Gomperts, R.; Mennucci, B.; Hratchian, H. P.; Ortiz, J. V.; Izmaylov, A. F.; Sonnenberg, J. L.; Williams-Young, D.; Ding, F.; Lipparini, F.; Egidi, F.; Goings, J.; Peng, B.; Petrone, A.; Henderson, T.; Ranasinghe, D.; Zakrzewski, V. G.; Gao, J.; Rega, N.; Zheng, G.; Liang, W.; Hada, M.; Ehara, M.; Toyota, K.; Fukuda, R.; Hasegawa, J.; Ishida, M.; Nakajima, T.; Honda, Y.; Kitao, O.; Nakai, H.; Vreven, T.; Throssell, K.; Montgomery, J. A., Jr.; Peralta, J. E.; Ogliaro, F.; Bearpark, M. J.; Heyd, J. J.; Brothers, E. N.; Kudin, K. N.; Staroverov, V. N.; Keith, T. A.; Kobayashi, R.; Normand, J.; Raghavachari, K.; Rendell, A. P.; Burant, J. C.; Iyengar, S. S.; Tomasi, J.; Cossi, M.; Millam, J. M.; Klene, M.; Adamo, C.; Cammi, R.; Ochterski, J. W.; Martin, R. L.; Morokuma, K.; Farkas, O.; Foresman, J. B.; Fox, D. J.*Gaussian 16* Rev. A.03; Gaussian, Inc.: Wallingford CT, 2016.
(50) Field, M. J.; Bash, P. A.; Karplus, M. A combined quantum mechanical and molecular mechanical potential for molecular dynamics simulations. *J. Comput. Chem.* **1990**, *11*, 700−733.
(51) Laidler, K. J.; King, M. C. Development of transition-state theory. *J. Phys. Chem.* **1983**, *87*, 2657−2664.
(52) Pechukas, P. Transition State Theory. *Annu. Rev. Phys. Chem.* **1981**, *32*, 159−177.
(53) Sasaki, S.; Suzuki, S.; Sameera, W. M. C.; Igawa, K.; Morokuma, K.; Konishi, G. Highly Twisted *N,N*-Dialkylamines as a Design Strategy to Tune Simple Aromatic Hydrocarbons as Steric Environment-Sensitive Fluorophores. *J. Am. Chem. Soc.* **2016**, *138*, 8194−8206.
(54) Peng, Z.; Wang, Z.; Tong, B.; Ji, Y.; Shi, J.; Zhi, J.; Dong, Y. Anthracene Modified by Aldehyde Groups Exhibiting Aggregation-Induced Emission Properties. *Chin. J. Chem.* **2016**, *34*, 1071−1075.
(55) Liu, M.; Onchaiya, S.; Tan, L. Y. F.; Haghighatbin, M. A.; Luu, T.; Owyong, T. C.; Hushiarian, R.; Hogan, C. F.; Smith, T. A.; Hong, Y. 9-Vinylanthracene Based Fluorogens: Synthesis, Structure-Property Relationships and Applications. *Molecules* **2017**, *22*, 2148.
(56) Sasaki, S.; Igawa, K.; Konishi, G. The effect of regioisomerism on the solid-state fluorescence of bis(piperidyl) anthracenes: structurally simple but bright AIE luminogens. *J. Mater. Chem. C* **2015**, *3*, 5940−5950.

https://doi.org/10.1021/acs.jctc.5c00231
J. Chem. Theory Comput. 2025, 21, 4992−5002